KIC 7284688: A Solar-type Eclipsing Binary with Rapidly Varying O'Connell Effect

Yang Pan[1] and Xiaobin Zhang[2]
[1] School of Physics and Astronomy, China West Normal University, Nanchong 637002, People's Republic of China; pyncxh@126.com
[2] Key Laboratory of Optical Astronomy, National Astronomical Observatories, Chinese Academy of Sciences, Beijing 100012, People's Republic of China

Abstract

We present comprehensive photometric and spectroscopic study of the short-period eclipsing binary KIC 7284688 based on the Kepler, TESS, and LAMOST data. The radial-velocity analysis indicates that it is a triple-lined system composed of a nearly equal-mass binary plus a line-of-sight star. The masses and radii of the components in the binary are measured to be $M_1 = 1.142 \pm 0.020 M_\odot$, $R_1 = 1.204 \pm 0.051 R_\odot$, and $M_2 = 1.119 \pm 0.019 M_\odot$, $R_2 = 1.149 \pm 0.052 R_\odot$. In addition to the eclipses, the light curves of the binary exhibit exhibit rapidly changing O'Connell effect, namely the inequality in light maxima, which could be attributed to the asynchronous rotation of the starspots. We analyzed the variability in the data of light residuals, the difference between light maxima (Max.I−Max.II) as well as the epochs of light minima and determined a rotation period of 0.644 days. Moreover, we detected a quasiperiod with ∼213 days from both the data of (Max.I−Max.II) and light times of minima, which is almost identical to the beat between the rotation period (∼0.644 days) and the orbital period (∼0.646 days). We conclude that the quasiperiodic variations of the O'Connell on the system are probably related to the starspot migration and this is a very rapid variation compared to the magnetic cycles with timescales ranging from years to decades.

Unified Astronomy Thesaurus concepts: Eclipsing binary stars (444); Stellar rotation (1629); Starspots (1572)

1. Introduction

O'Connell effect (O'Connell 1951), the inequality in the two out-of-eclipse light maxima (Max.I and Max.II at orbital phase ∼0.25, ∼0.75, respectively), is common on late-type eclipsing binaries (EBs), e.g., RS Cvn-type, Algol-type, and W UMa-type EBs. In some systems the O'Connell effect is relatively stable, but appears to quasiperiodic variation in others (Wilsey & Beaky 2009; Sriram et al. 2017) and the variation timescale vary from a few years to decades. Usually, starspot activity is proposed to explain the inequality (Knote et al. 2022). For instance, the evolution of the inequality on a RS Cvn-type binary KOI-1003 was simulated by Roettenbacher et al. (2016) using the evolution of persistent starspots at two longitudes. The periodic variation of the inequality with a cycle length of ∼2000 days detected in Algol-type binary KIC 06852488 was interpreted by Shi et al. (2021) using two-spot model. The quasiperiodic rapid variation (∼40 days) of the inequality on a W UMa-type binary system HH UMa was explained by Wang et al. (2015) using flip-flop cycle. So far, most of these studies on the phenomenon focus on semidetached and contact binaries with ground-based photometry. We lack an understanding of double-lined detached EBs with high-precision, continuous photometry.

Kepler Mission (Borucki et al. 2010) provides an excellent opportunity for this field study. Kepler discovered nearly 3000 EBs at a high-precision photometric level (Kirk et al. 2016), of which ∼200 EBs have obvious O'Connell effect (Knote et al. 2022). The follow-up time-domain medium-resolution LAMOST-Kepler spectroscopic observations (LK-MRS; Wilson 2020), which are as part of LAMOST-Kepler (LK) survey (De Cat et al. 2015; Zong et al. 2018; Fu et al. 2020, 2022), have led to the discovery of lots of double-lined

spectroscopic binary, and a few triple-lined systems (Frasca et al. 2022). Therefore, the combination between those two observations contributes to derive fundamental physical parameters of these systems and explore the O'Connell effect.

KIC 7284688 is labeled as an Algol-type EB with an orbital period of $P_{\rm orb} = 0.6460432$ days in the Kepler Eclipsing Binary Catalog (Prša et al. 2011; Slawson et al. 2011; Kirk et al. 2016, KEBC). Conroy et al. (2014) found that the eclipse timing variations (also referred to as the Observed minus Computed ($O−C$)) curves for the primary and secondary eclipses are anticorrelated, which can be explained by starspot activity. Lurie et al. (2017) detected two rotation periods ($P_{1 \min} \approx 0.643$ day, $P_{1 \max} \approx 0.648$ day) from the out-of-eclipse fluctuations due to starspot activity. A total of 26 flares is detected by Gao et al. (2016). Moreover, KIC 7284688 is identified as a spectroscopic triple-lined system by Frasca et al. (2022). In addition, KIC 7284688 (=TIC 63368767, $T_{\rm mag} = 11.008$) was also observed by Transiting Exoplanet Survey Satellite (TESS; Ricker et al. 2015) at a 2 minutes cadence in Sector 15 on August 2019, Sector 40, 41 on 2021 June and July, respectively, and Sector 54, 55 on 2022 July and August, respectively.

This article is organized as follows. In Section 2, we present the Kepler, TESS and LAMOST observations. In Section 3, a binary modeling is carried out to measure physical properties of KIC 7284688. In Section 4, we analyze the periodic signatures in the out-of-eclipse residuals, in the $O−C$ diagrams and in the difference between the two maxima (Max.I−Max.II), and discuss the results in Section 5. Finally, Section 6 gives a summary.
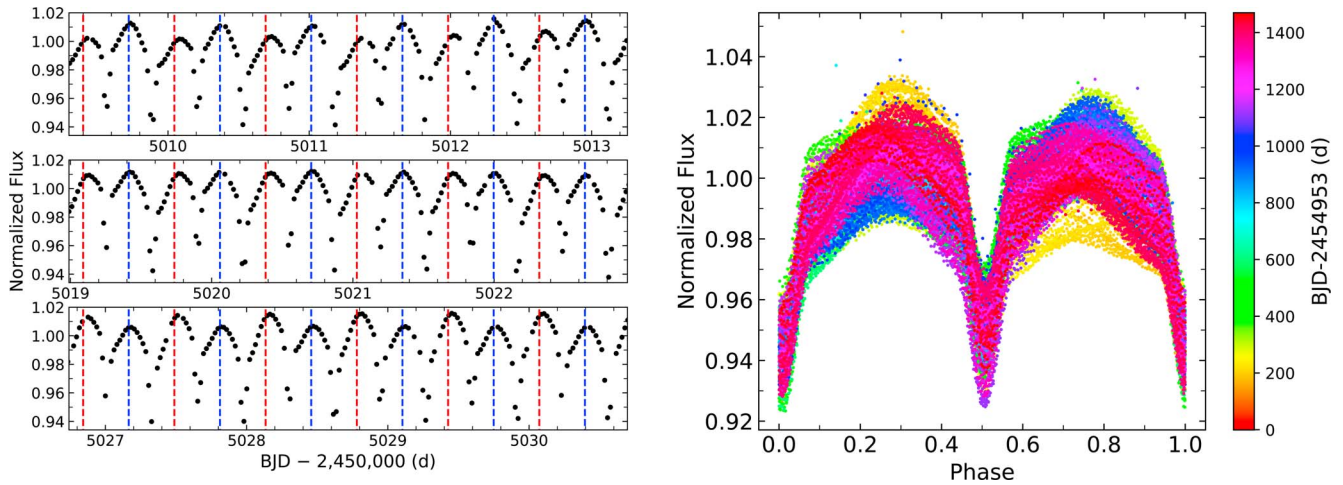
2. Space-based Photometry and LAMOST Spectroscopy

2.1. Space-based Photometry

KIC 7284688 was observed by Kepler with long-cadence mode (29.4 minutes sampling) from Quarters Q0 through Q17. The contamination factors from the Mikulski Archive for Space

Figure 1. Left panel: a 12 day segment of the normalized light curve of KIC 7284688 from Q2. The times corresponding to orbital phase at 0.25 and 0.75 are marked by the red and blue dashed lines, respectively. Right panel: the phased Kepler light curve of KIC 7284688 evolving with time represented by the color in the color bar.

Telescopes (MAST[3]) are smaller than 0.2%. In this study, the simple aperture photometry (SAP) light curves downloaded from the MAST are used. The SAP light curves are detrended using a similar method described in Fetherolf et al. (2019). Briefly, the SAP data was separated by observation gaps (>1 days) into many segments. Then, to remove instrumental trends, a low-order polynomial was used to fit the out-of-eclipse portion of each segment. The left panel of Figure 1 shows a 12 day segment of the detrended and normalized light curve from Q2 and the red and blue dashed lines mark, respectively, the times corresponding to orbital phase at 0.25 and 0.75, which were calculated from the linear ephemeris (Min.I = 2454953.678043 + 0.6460432 × E) given by KEBC. A variable inequality in maxima near quadrature phase can be found. Initially, in the top panel, the light maximums (Max.I) near the red dashed lines are fainter than the light maximums (Max.II) near the blue dashed lines. Then, the Max. I is almost equal to Max.II in the middle panel. After some time, the Max.I become brighter than Max.II in the bottom panel (see Section 4.3 for the calculation of the Max.I and Max. II). More specifically, the right panel of Figure 1 displays the phase-folded long-cadence light curves from Q0-17 evolving with time. In addition, KIC 7284688 was also observed by TESS at 2 minutes cadence. The light curves in Sector 15, 40, 41, 54, 55 are downloaded from the MAST and the PDCSAP flux data are directly used. By using the linear ephemeris, we calculate orbital phases of the data and the averages of the flux between orbital phase 0.24–0.26 in each sector. The normalized light curves are obtained by dividing the average values and are shown in Figure 2. Obviously, the TESS light curves are variable, especially in the depth of the secondary eclipse between Sector 15 and Sector 55 and in the out-of-eclipse shape following the secondary eclipse. Moreover, a flare can be also found in Sector 15 at nearby orbital phase of 0.65. Therefore, the inequality in maxima can be related to stellar activity.

2.2. LAMOST Spectroscopy

KIC 7284688 was observed by LK survey in low-resolution and medium-resolution mode. The spectral resolution and wavelength range are $R \sim 1800$ and 370–900 nm for the low-resolution mode, and, in the medium-resolution mode, the spectral resolution is $R \sim 7500$, and the wavelength range is 495–535 nm and 630–680 nm. In total, four low-resolution spectra and 71 medium-resolution ones with signal-to-noise ratios in the range 24–85 were obtained. The atmospheric parameters from the low-resolution spectrum at the orbital phase of about 0.51 were provided in LAMOST DR9[4] as, $T_{\mathrm{eff}} = 5696 \pm 27$K, $\log g = 4.33 \pm 0.04$, [Fe/H] $= 0.21 \pm 0.02$. Radial velocities (RVs) from the medium-resolution spectra were extracted using the broadening function (BF) technique developed by Rucinski (2002, 2004). Briefly, BFs were extracted using the observed solar spectrum (Kurucz et al. 1984) as the template. Then, RVs were measured using Gaussian functions to fit the peaks in the BFs. In 46 out of the 71 spectra, the BFs show three apparent peaks, a higher peak in the middle and smaller peaks on each side, suggesting that the spectra are triple-lined. The remaining are double-lined or single-lined spectra because these are observed at conjunction phases. As an example, Figure 3 display representative BF and the corresponding triple Gaussian fitting.

Due to RV zero-points of standard stars vary between exposures in LAMOST Medium-resolution Survey (Zhang et al. 2021; Pan et al. 2022), similar to differential photometry, we apply differential radial velocity to correct zero-point offset among RVs. Two candidates of RV standard stars with standard deviations of absolute RVs less than 1.0 km s^{-1} from Zhang et al. (2021) are selected as the comparison ($\alpha_{J2000.0} = 292°.1127$, $\delta_{J2000.0} = 43°.3892$, $RV = 0.86 \pm 0.34$ km s^{-1}) and check ($\alpha_{J2000.0} = 292°.5231$, $\delta_{J2000.0} = 43°.3609$, $RV = 1.10 \pm 0.29$ km s^{-1}) stars, respectively. With the same BF method, the RVs of the two stars are determined. The differential RVs (v_1, v_2, v_3) of the triple-lined system are listed in Table 1, and the RV uncertainties are estimated by using a Monte Carlo simulation (Li et al. 2021). The subscripts 1, 2, and 3, respectively, correspond to the primary, secondary, and the third component. With the linear ephemeris from the KEBC, the phased RVs are displayed in Figure 4.
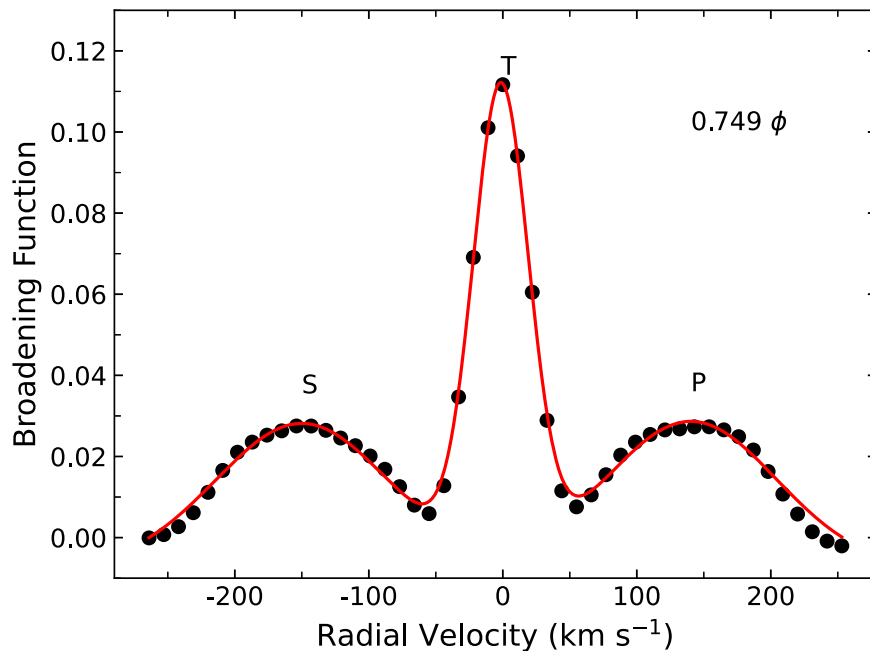
The phased RVs of the third component (red triangle) shown in Figure 4 are roughly constant. This suggests it may be a line-of-sight coincident source. In addition, since the areas under the

---
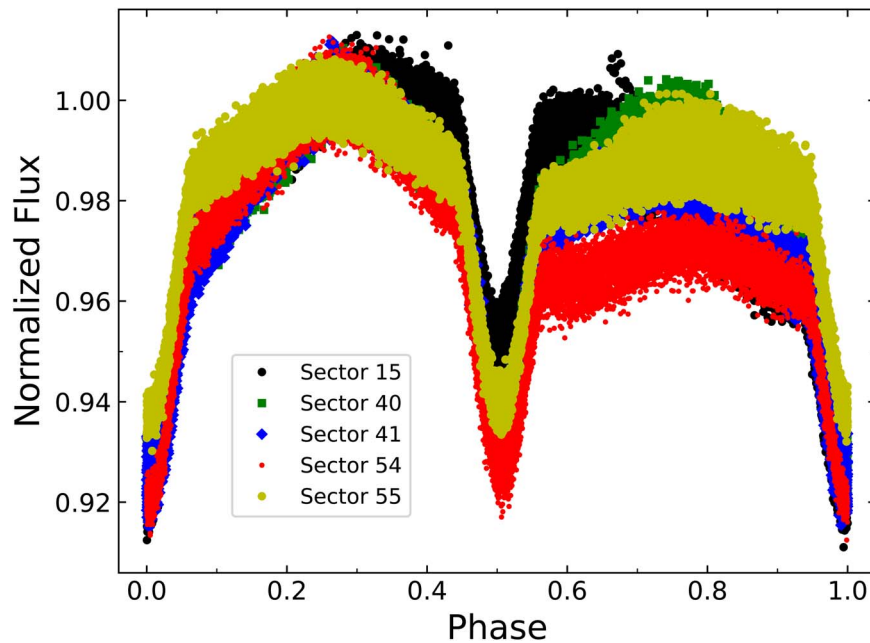
Figure 2. The normalized and phased TESS light curves from Sector 15 (black points), Sector 40 (green squares), Sector 41 (blue diamonds), Sector 54 (red points), Sector 55 (yellow points).

Figure 3. The BF (black points) and the Gaussian fits (red lines). The abscissa is is radial velocity on the heliocentric frame. The vertical axis is arbitrary amplitude of the BF. The orbital phase, and the peaks due to the primary (p), the secondary (s), and the third component (T) are indicated.

BFs of the three peaks in Figure 3 at quadrature phase are comparable, the third component is not a faint source.

3. Binary Modeling

To determine the properties of KIC 7284688, the Wilson–Devinney (WD, 2013) code (Wilson & Devinney 1971; Wilson 1979, 1990, 2012) is used to model the Kepler light curves plus the LAMOST RVs and the TESS light curves plus the LAMOST RVs, respectively. Considering the short orbital period, a circular orbital with synchronous rotation for both components is assumed in our model. To derive the ratio of semiamplitudes (K_1/K_2), namely mass ratio ($q = m_2/m_1 = K_1/K_2$), the LAMOST RVs are fitted by Kepler circular orbit. The mass ratio is determined to be $q = 0.980 \pm 0.004$. Therefore, the mass ratio was fixed to be 0.980 in our model. According to the atmospheric parameters given by the LAMOST low-resolution spectrum at conjunction phase, the primary temperature was set to be $T_1 = 5696 \, K$. For late-type stars with convective envelopes, the bolometric albedos (Ruciński 1969) and the gravity-darkening exponents (Lucy 1967) were set to 0.5 and 0.32, respectively. The bolometric limb-darkening coefficients with logarithmic form

Table 1
KIC 7284688 Radial-velocity Measurements

Time (BJD−2,450,000)	Orbital (Phase)	V_1 (km s^{-1})	V_2 (km s^{-1})	V_3 (km s^{-1})
8263.26993	0.8647	115.10 ± 2.31	−119.33 ± 4.87	3.65 ± 0.15
8263.28313	0.8851	98.69 ± 4.69	−89.54 ± 3.49	4.26 ± 0.14
8263.29563	0.9045			4.09 ± 0.52
8263.30882	0.9249			3.42 ± 0.55
8263.32132	0.9442			2.97 ± 0.2
8267.22634	0.9887			5.59 ± 0.27
8267.23884	0.0081			4.83 ± 0.28
8267.25204	0.0285			4.54 ± 0.33
8267.26454	0.0479			5.03 ± 0.20
8267.27704	0.0672			5.08 ± 0.24
8267.29023	0.0876			4.44 ± 0.36
8267.31037	0.1188		105.28 ± 5.43	3.33 ± 0.77
8268.23541	0.5507			4.84 ± 0.30
8268.24513	0.5657			5.15 ± 0.24
8268.25416	0.5797			4.74 ± 0.36
8268.26319	0.5937			5.40 ± 0.28
8268.27291	0.6087			5.77 ± 0.34
8268.28263	0.6238	103.63 ± 2.21	−86.37 ± 5.99	5.02 ± 0.38
8268.29166	0.6377	106.26 ± 3.61	−116.6 ± 16.49	5.36 ± 0.40
8268.30347	0.6560	120.70 ± 3.62	−111.05 ± 2.42	5.3 ± 0.36
8268.31319	0.6711	123.90 ± 2.15	−124.84 ± 5.57	5.01 ± 0.90
8269.25072	0.1223		106.85 ± 1.31	4.68 ± 0.52
8269.26461	0.1438	−122.13 ± 15.35	120.97 ± 1.34	3.38 ± 0.34
8269.27781	0.1642	−119.48 ± 4.96	127.08 ± 1.83	3.71 ± 0.90
8269.29031	0.1835	−126.88 ± 8.29	135.81 ± 2.35	6.03 ± 0.57
8269.30350	0.2039	−136.42 ± 2.73	140.96 ± 6.97	3.57 ± 0.58
8270.25354	0.6745	128.36 ± 2.62	−126.47 ± 4.50	4.73 ± 0.76
8270.26951	0.6992	138.97 ± 1.36	−135.24 ± 1.28	4.89 ± 0.80
8270.28618	0.7250	142.97 ± 1.81	−139.87 ± 1.66	3.27 ± 0.76
8270.30215	0.7497	144.88 ± 1.71	−145.52 ± 1.24	3.05 ± 0.16
8625.27118	0.2007	−137.08 ± 1.46	141.51 ± 7.1	5.53 ± 0.11
8625.28716	0.2254	−138.82 ± 1.51	140.29 ± 9.2	5.51 ± 0.13
8625.30382	0.2512		151.57 ± 2.93	8.11 ± 0.35
8644.22538	0.5396			3.97 ± 0.65
8644.24205	0.5654			4.56 ± 0.15
8644.25802	0.5901			4.66 ± 0.15
8644.27399	0.6148	94.60 ± 2.27	−80.20 ± 5.59	5.18 ± 0.67
8646.24489	0.6655	126.45 ± 2.02	−117.05 ± 1.61	5.09 ± 0.15
8646.26086	0.6903	137.81 ± 2.14	−128.14 ± 2.05	4.91 ± 0.13
8646.28378	0.7257	148.38 ± 2.24	−134.12 ± 2.98	5.13 ± 0.32
9001.22577	0.1348	−101.61 ± 4.59	109.00 ± 7.28	2.99 ± 0.49
9001.25355	0.1778	−131.72 ± 1.89	132.69 ± 2.91	3.18 ± 0.16
9001.27161	0.2057	−138.09 ± 2.13	136.21 ± 5.16	3.00 ± 0.19
9001.28758	0.2305	−138.06 ± 2.88	147.00 ± 3.59	2.73 ± 0.30
9001.30425	0.2563	−139.32 ± 2.77		1.52 ± 0.49
9003.21960	0.2210	−130.3 ± 13.67	146.81 ± 4.49	4.72 ± 0.30
9003.23557	0.2457	−142.07 ± 2.54	138.11 ± 4.05	4.00 ± 0.21
9003.25154	0.2704	−134.80 ± 3.86	134.52 ± 4.53	4.00 ± 0.78
9003.26821	0.2962	−134.34 ± 1.55	136.48 ± 4.07	4.65 ± 0.18
9003.28418	0.3210	−131.49 ± 2.49	126.22 ± 5.86	2.57 ± 0.34
9003.30015	0.3457	−109.77 ± 3.41	115.44 ± 8.63	4.62 ± 0.88
9004.23769	0.7969	137.48 ± 1.43	−141.57 ± 2.21	3.29 ± 0.21
9004.25366	0.8216	138.34 ± 4.14	−131.36 ± 2.37	3.44 ± 0.20
9004.26963	0.8463	120.82 ± 4.65	−105.32 ± 4.87	4.54 ± 0.29
9004.28630	0.8721	106.13 ± 4.28	−100.39 ± 12.37	4.07 ± 0.30
9004.30227	0.8969			3.62 ± 0.41
9006.29124	0.9755			2.58 ± 0.18
9011.25530	0.6593	115.71 ± 9.07	−129.82 ± 9.6	3.59 ± 0.98
9011.27196	0.6851	128.97 ± 2.30	−153.09 ± 6.94	3.35 ± 0.58
9011.28794	0.7099	150.62 ± 8.88	−149.7 ± 2.49	3.04 ± 0.55
9011.30460	0.7357	141.57 ± 4.35	−163.56 ± 9.57	3.53 ± 0.37
9015.19917	0.7640	146.92 ± 2.76	−143.13 ± 2.3	4.50 ± 0.32
9015.21515	0.7887	137.27 ± 1.68	−140.13 ± 1.64	2.56 ± 0.59

Table 1
(Continued)

Time (BJD−2,450,000)	Orbital (Phase)	V_1 (km s^{-1})	V_2 (km s^{-1})	V_3 (km s^{-1})
9015.23181	0.8145	131.21 ± 9.12	-134.75 ± 1.53	3.36 ± 0.14
9015.25473	0.8500	115.12 ± 2.62	-115.02 ± 2.28	3.33 ± 0.22
9015.27140	0.8758	91.08 ± 2.49	-113.30 ± 2.22	3.58 ± 0.18
9015.28737	0.9005			3.25 ± 0.29
9016.24226	0.3786	-89.46 ± 5.10	95.72 ± 7.81	2.43 ± 0.58
9016.25893	0.4044	-80.20 ± 2.67		3.36 ± 0.52
9016.27490	0.4291			2.51 ± 0.24
9016.29157	0.4549			3.28 ± 0.18
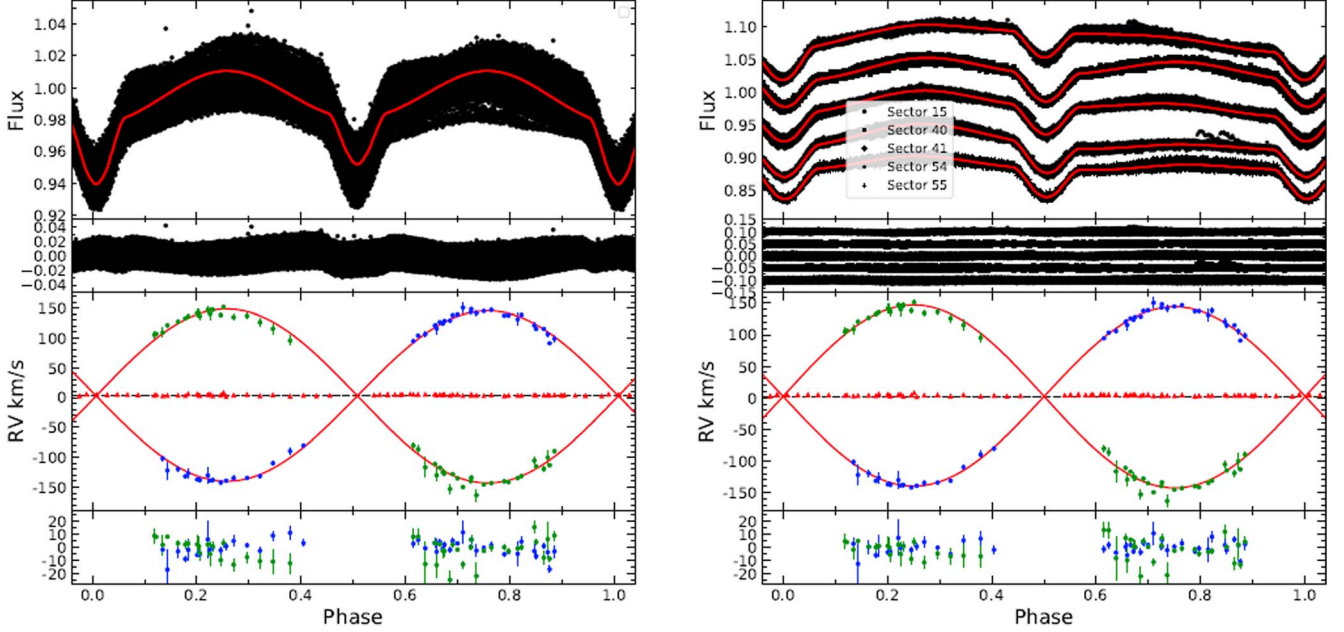
Figure 4. Left panel: top panel: the phased Kepler light curve and the best-fit WD model. Second panel: the residuals after fitting the Kepler light curve. Third panel: the phased RVs of the primary (blue points), the secondary (green points), the third component (red triangles), and the best-fit WD model (red solid lines). The systemic velocities of the binary are indicated by black dashed line. Bottom panel: the residuals after fitting the primary and the secondary RVs. Right panel: top panel: the phased TESS light curves from Sector 15 (black points), 40 (black squares), 41 (black diamonds), 54 (black stars), 55 (black pluses), and the best-fit WD models (red solid lines). For better visualization, the normalized light curves are shifted up and down by 0.1 for sectors 15, 55, and by 0.05 for sectors 40, 54, respectively. Second panel: the corresponding residuals after fitting the TESS light curves. Third panel: the phased RVs of the primary (blue points), the secondary (green points), the third component (red triangles), and the best-fit WD model (red solid lines). The systemic velocities of the binary are indicated by black dashed line. Bottom panel: the residuals after fitting the primary and the secondary RVs.

were interpolated from van Hamme (1993). For Kepler and TESS band, the monochromatic coefficients were interpolated from WD code and Claret (2017), respectively.

Considering that KIC 7284688 is categorized as an EA-type eclipsing binary in KEBC 1 and KEBC 2, yet, its morphological parameter in the 3rd KEBC is 0.64, these imply that it is likely an EA or EB-type system. Therefore, to model the Kepler light curves and the LAMOST RVs, the mode 2 (detached binary), mode 4 (semidetached binary with the primary filling its Roche lobe), and mode 5 (semidetached binary with the secondary filling its Roche lobe) in the WD code were applied. In addition, two models were used to derive the physical parameters of the system. The first is a model without a third light, and the second is a model with it. In the second model, since the third component is not a faint source, the third light of $l_3 = 0.3$ is assumed. The free parameters of the models are as follows: the inclination (i), the semimajor axis of the binary (a), the dimensionless surface potential of the stars ($\Omega_{1,2}$ for mode 2, Ω_2 for mode 4, Ω_1 for mode 5), the center-of-

mass velocity (γ), the secondary temperature (T_2), the dimensionless primary luminosity (L_1), and the phase shift.

The solutions converged in the mode 2 and mode 5. However, the fits in the mode 5 are worse than the ones in the mode 2, indicating that KIC 7284688 is detached binary. The parameters obtained from the solutions of mode 2 without and with third light are given in Tables 2 and 3, respectively. The theoretical light and RV curves (red lines), along with the center-of-mass velocity of the binary and the corresponding $O-C$ residuals, are displayed in left panel of Figure 4.

To model the TESS light curves and the LAMOST RVs, only the mode 2 with or without third light was used. To model the inequality in the TESS light curves, two spots located on the primary are assumed. Therefore, the spot parameters (colatitude, longitude, spot angular radius, and temperature factor) are also adjustable. Since there exists degeneracy among spot parameters, we fixed the colatitude of each spot to be 90°. In each model, the five phased light curves in Sector 15, 40, 41, 54, 55 as the input, respectively. A summary of the results of

Table 2
Parameters from Binary Modeling without Third Light

	Kepler	Sector 15	Sector 40	Sector 41	Sector 54	Sector 55
$q = M_2/M_1$ (fixed)	0.98	0.98	0.98	0.98	0.98	0.98
i (deg)	63.818 ± 0.049	63.679 ± 0.038	62.199 ± 0.022	62.046 ± 0.023	62.747 ± 0.023	62.932 ± 0.024
T_1 (K) (fixed)	5696	5696	5696	5696	5696	5696
T_2 (K)	5323 ± 172	5320 ± 172	5734 ± 172	5725 ± 172	5598 ± 172	5635 ± 172
Ω_1	4.698 ± 0.015	4.4726 ± 0.0012	4.349 ± 0.008	4.335 ± 0.008	4.572 ± 0.008	4.400 ± 0.008
Ω_2	4.742 ± 0.018	4.771 ± 0.017	4.525 ± 0.010	4.504 ± 0.010	4.372 ± 0.007	4.604 ± 0.009
γ(km s^{-1})	2.71 ± 0.62	2.25 ± 0.54	2.39 ± 0.56	2.40 ± 0.56	2.44 ± 0.57	2.45 ± 0.57
a($R_\odot$)	4.103 ± 0.020	4.091 ± 0.017	4.150 ± 0.018	4.156 ± 0.018	4.131 ± 0.019	4.125 ± 0.019
M_1 ($M_\odot$)	1.122 ± 0.020	1.113 ± 0.020	1.162 ± 0.020	1.167 ± 0.020	1.146 ± 0.020	1.141 ± 0.020
M_2 ($M_\odot$)	1.100 ± 0.019	1.091 ± 0.019	1.139 ± 0.019	1.144 ± 0.019	1.124 ± 0.019	1.118 ± 0.019
R_1 ($R_\odot$)	1.118 ± 0.051	1.191 ± 0.051	1.256 ± 0.051	1.263 ± 0.051	1.168 ± 0.051	1.228 ± 0.051
R_2 ($R_\odot$)	1.091 ± 0.052	1.079 ± 0.052	1.176 ± 0.052	1.185 ± 0.052	1.227 ± 0.052	1.141 ± 0.052
l3 (fixed)	0	0	0	0	0	0
Spot1						
Colatitude (deg) (fixed)	⋯	90	90	90	90	90
Longitude (deg)	⋯	290.05 ± 0.40	301.01 ± 0.47	295.98 ± 0.48	294.67 ± 0.73	277.61 ± 0.39
Radius (deg)	⋯	78.85 ± 0.97	50.44 ± 0.51	54.73 ± 0.79	95.17 ± 1.08	57.27 ± 1.05
Temp.factor	⋯	. 0.9782 ± 0.0001	0.9793 ± 0.0001	0.9814 ± 0.0001	0.9815 ± 0.0001	0.9805 ± 0.0001
Spot2						
Colatitude (deg) (fixed)	⋯	90	90	90	90	90
Longitude (deg)	⋯	80.85 ± 0.27	83.97 ± 0.31	78.97 ± 0.31	97.26 ± 0.40	91.09 ± 0.21
Radius (deg)	⋯	52.18 ± 0.23	35.45 ± 0.27	36.03 ± 0.26	47.30 ± 0.18	34.71 ± 0.35
Temp.factor	⋯	0.9521 ± 0.0001	0.9605 ± 0.0001	0.9377 ± 0.0001	0.9386 ± 0.0001	0.9379 ± 0.0001

Table 3
Parameters from Binary modeling with third light

	Kepler	Sector 15	Sector 40	Sector 41	Sector 54	Sector 55
$q = M_2/M_1$	0.98	0.98	0.98	0.98	0.98	0.98
i (deg)	65.438 ± 0.06	65.816 ± 0.049	65.639 ± 0.037	65.714 ± 0.032	66.135 ± 0.045	65.748 ± 0.023
T_1 (K) (fixed)	5696	5696	5696	5696	5696	5696
T_2 (K)	5339 ± 123	5383 ± 123	5646 ± 123	5644 ± 123	5577 ± 123	5601 ± 123
Ω_1	4.557 ± 0.011	4.352 ± 0.0011	4.191 ± 0.006	4.184 ± 0.006	4.177 ± 0.007	4.459 ± 0.008
Ω_2	4.805 ± 0.014	5.011 ± 0.022	5.179 ± 0.013	5.222 ± 0.011	5.193 ± 0.017	4.782 ± 0.010
γ(km s^{-1})	2.72 ± 0.51	2.33 ± 0.54	2.40 ± 0.56	2.41 ± 0.56	2.45 ± 0.57	2.45 ± 0.57
a($R_\odot$)	4.048 ± 0.020	4.023 ± 0.017	4.030 ± 0.017	4.028 ± 0.017	4.017 ± 0.018	4.029 ± 0.018
M_1 ($M_\odot$)	1.078 ± 0.007	1.058 ± 0.007	1.064 ± 0.007	1.063 ± 0.007	1.054 ± 0.007	1.063 ± 0.007
M_2 ($M_\odot$)	1.056 ± 0.007	1.037 ± 0.007	1.043 ± 0.007	1.041 ± 0.007	1.032 ± 0.007	1.042 ± 0.007
R_1 ($R_\odot$)	1.149 ± 0.056	1.216 ± 0.056	1.284 ± 0.056	1.287 ± 0.056	1.286 ± 0.056	1.178 ± 0.056
R_2 ($R_\odot$)	1.058 ± 0.049	0.995 ± 0.049	0.956 ± 0.049	0.945 ± 0.049	0.949 ± 0.049	1.060 ± 0.049
l3 (fixed)	0.3[a]	0.3[a]	0.3[a]	0.3[a]	0.3[a]	0.3[a]
Spot1						
Colatitude (deg) (fixed)	⋯	90	90	90	90	90
Longitude (deg)	⋯	283.49 ± 0.67	309.89 ± 1.35	304.14 ± 1.39	295.73 ± 1.72	281.61 ± 0.59
Radius (deg)	⋯	69.67 ± 1.2	37.09 ± 0.45	36.52 ± 0.61	30.28 ± 0.91	38.81 ± 0.50
Temp.factor	⋯	. 0.9766 ± 0.0001	0.9797 ± 0.0001	0.9817 ± 0.0001	0.9814 ± 0.0001	0.9804 ± 0.0001
Spot2						
Colatitude (deg) (fixed)	⋯	90	90	90	90	90
Longitude (deg)	⋯	67.71 ± 0.43	85.88 ± 0.49	75.96 ± 0.38	90.66 ± 0.26	93.15 ± 0.26
Radius (deg)	⋯	52.83 ± 0.46	27.54 ± 0.32	30.56 ± 0.21	35.06 ± 0.24	29.53 ± 0.18
Temp.factor	⋯	0.9445 ± 0.0001	0.9606 ± 0.0001	0.9372 ± 0.0001	0.9380 ± 0.0001	0.9382 ± 0.0001

Note.
[a] assumed.

the two models is given in Tables 2 and 3. Since the errors of the free parameters from WD code are underestimated (Prša & Zwitter 2005), we estimated the uncertainties of the absolute physical properties using the standard deviation of these outputs. The fitted light and RV curves (red lines), the center-of-mass velocity of the binary, and the corresponding

$O-C$ residuals are shown in the right panel of Figure 4. For a better display, the normalized light curves and the corresponding residuals are shifted up and down by 0.1 for sectors 15 and 55, and by 0.05 for sectors 40 and 54, and only one RV fit is shown. The phased RVs of the third component (red triangle) are almost constant and are very close to the systemic velocity (black dashed line) of the eclipsing pair.

In Table 2 (with $l_3 = 0$) and Table 3 (with $l_3 = 0.3$), the maximal relative differences of the parameters, $(P_{\mathrm{Kepler}} - P_{\mathrm{Sector}})/P_{\mathrm{Kepler}}$, is less than 5% with an exception of the relative difference of the radius of the secondary star $(R_{2\,\mathrm{Kepler}} - R_{2\,\mathrm{Sector}54})/R_{2\,\mathrm{Kepler}} \sim 12\%$. Therefore, the absolute parameters derived from Kepler data are basically consistent with ones from TESS data. In addition, since most of the relative differences of the parameters is less than 5%, the model results for different TESS sectors are also basically consistent with each other. These hint that for short-period EBs, the parameters derived from Kepler long-time-series data are reliable although the Kepler 30 minutes sampling is more sparse than the TESS 2 minutes sampling. The consistency between models corresponding to the different sectors increases the reliability of model results. Besides, although, the masses and the radii of the secondary in Table 2 are slightly larger than ones in Table 3, the two models yield similar and acceptable results. Therefore, only according to the results, it is difficult to identify whether the third component belongs to a triple system and which model is the favored one. Considering that the RVs of the third component are close to zero and constant, the third component could be a line-of-sight coincident source. Therefore, we infer that KIC 7284688 is a close binary composed of two solar-type stars and the averaged values of masses and radii in Table 2 are regarded as the masses and radii of the both components, namely $M_1 = 1.142 \pm 0.020 M_\odot$, $R_1 = 1.204 \pm 0.051 R_\odot$, and $M_2 = 1.119 \pm 0.019 M_\odot$, $R_2 = 1.149 \pm 0.052 R_\odot$.

4. Periodic Signatures

In this section, we analyze the periodicities in the out-of-eclipse flux residuals, in the $O-C$ diagram (namely the residuals of the Kepler mideclipse time measurements), and in the O'Connell effect, respectively.

4.1. Periodicities in Out-of-eclipse Flux Residuals

The out-of-eclipse light variations are from the binary and starspot modulations. To obtain the variations from starspot modulations, the binary models without third light were used to produce the synthesized light curves. The out-of-eclipse flux residuals were obtained by subtracting the synthesized light curves from the Kepler and TESS detrended light curves. Since the light variations in the residuals are related to starspots, the spin period(s) of the starpot(s) can be measured from the residuals. The left panel of Figure 5 shows the Lomb–Scargle (LS) periodogram of the out-of-eclipse flux residuals for Kepler data, together with a zoom-in view around the orbital frequency of the binary (~ 1.547 day^{-1}). In the upper panel, several strong peaks (black lines) very close to the orbital frequency and orbital harmonics (red dashed lines) are detected. Obviously, in the lower panel, the frequencies of the three distinct peaks is slightly higher than the orbital frequency. This indicates that the spinning of the starspot is faster than the binary. The periods corresponding to the three distinct frequencies respectively are 0.6440, 0.6428, 0.6429 days. In comparison, we calculated the LS periodogram of the out-of-eclipse

residuals in Sector 15, Sector 40, 41, and Sector 54, 55, respectively, as shown in the right panel of Figure 5. Two frequencies are detected in the TESS residuals, which are almost symmetric about the orbital frequency and are slightly different from the frequencies in Kepler residuals. The symmetry of two frequencies may be related to differential rotation. The greater of the two frequencies could be ascribed to the starspots at low latitudes with rotating faster than the binary and the smaller could be attribute to the starspots at high latitudes with slower rotating.

### 4.2. Periodicities in the $O-C$ Diagram

Starspots can distort the shape of each eclipse, which causes the shift of mideclipse time (Fetherolf et al. 2019) and lead to the $O-C$ diagram to exhibit anticorrelated fluctuations for the primary and secondary eclipses. Using the eclipse time variations given by the KEBC, the anticorrelation is shown in the upper left of Figure 6 and there exists coherent deviations of about twenty minutes for the primary and secondary. The LS periodograms of the $O-C$ for the primary and secondary eclipses are respectively computed and displayed in the middle and bottom left panels of Figure 6. A quasiperiod of ~ 207 days is found in the periodograms of the primary and secondary $O-C$. In addition, for TESS data, we calculated the times of light minimum using the K-W method (Kwee & van Woerden 1956) and then the $O-C$ using the linear ephemeris given by KEBC, as shown in the right panel of Figure 6. Since there are long gaps between sectors and no obvious periodic signals, we did not computed the LS periodogram of the $O-C$ for TESS data.

4.3. Periodicities in the O'Connell Effect

In addition to shift the mideclipse time, starspots can also distort shape of out-of-eclipse light variation. As shown in Figure 1, the out-of-eclipse light curves are obvious inequality in maxima. At the beginning, the light maximums (Max.I) following the primary eclipses are fainter than the light maximums (Max.II) following the secondary ones. After some time, Max.I become brighter than Max.II. The phenomenon is regularly repeated at a later time. To better understand the variations, we calculated the values of Max.I and Max.II in each orbital cycle as follows. According to the widths of the primary and secondary eclipses (pwidth = 0.0980, swidth = 0.1008) in phase given in KEBC, the data in orbital phases 0.0735–0.4237 (phase I) and 0.5749–0.9265 (phase II) are isolated. The phase I and phase II data in each orbital cycle are then respectively fitted using a second order polynomial. The maximum values from the fitted curves in phase I and phase II are regarded as the Max.I and Max.II, respectively. Then we compute the differences between the maxima (Max.I−Max.II), and the LS periodogram of Max.I−Max.II. The left panel of Figure 7 shows the Max.I−Max.II evolving with time and its periodogram for Kepler data. A significant spike at ~ 213.01 days is detected in the periodogram of the Max.I−MaxII. Meanwhile, a spike at ~ 130 days is also detected, which can be related to the oscillation of the Max.I−Max.II between days 300 and 700 (BJD-2,455,000) shown in left upper panel of Figure 7. In addition, a fast oscillation (~ 50 days) of the Max.I−Max.II can be seen between days 1100 and 1200. In comparison, we calculated the Max.I−Max.II for TESS Sector 40, 41, 54, 55. (In Sector 15, the light curves following the secondary eclipse is decreasing, no obvious maxima can be
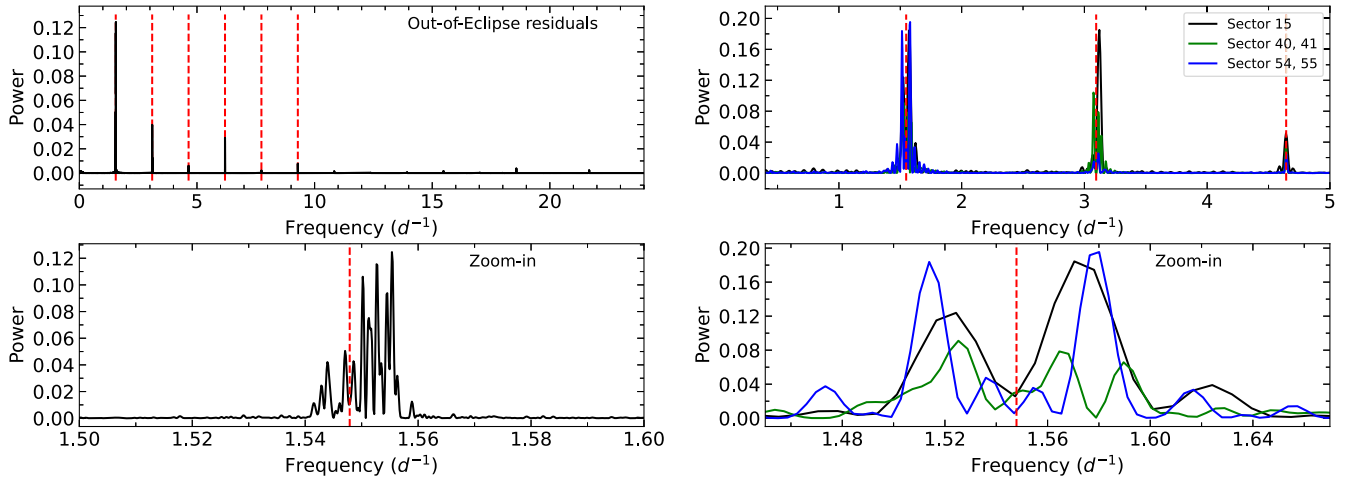
Figure 5. Left panel: the LS periodogram of the out-of-eclipse residuals for Kepler data (upper panel) and a zoom-in of the LS periodogram around the orbital frequency of the binary (lower panel). Right panel: the LS periodograms of the out-of-eclipse residuals for TESS Sector 15, Sector 40, 41 and Sector 54, 55 (upper panel), and a zoom-in of the LS periodograms around the orbital frequency of the binary (lower panel). The red dashed lines represent the orbital frequency of the binary and orbital harmonics.
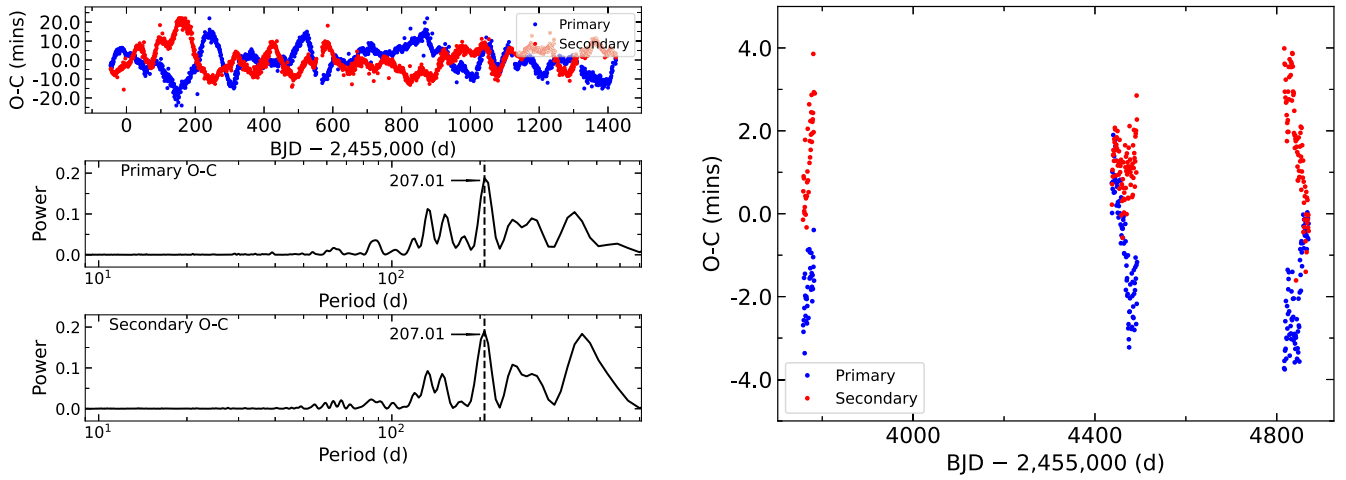
Figure 6. Left panel: the $O-C$ diagram for the primary and secondary eclipses given by KEBC (top panel), the LS periodogram of the primary $O-C$ (middle panel), and the LS periodogram of the secondary $O-C$ (bottom panel). Right panel: the $O-C$ diagram for the primary and secondary eclipses obtained from TESS data.
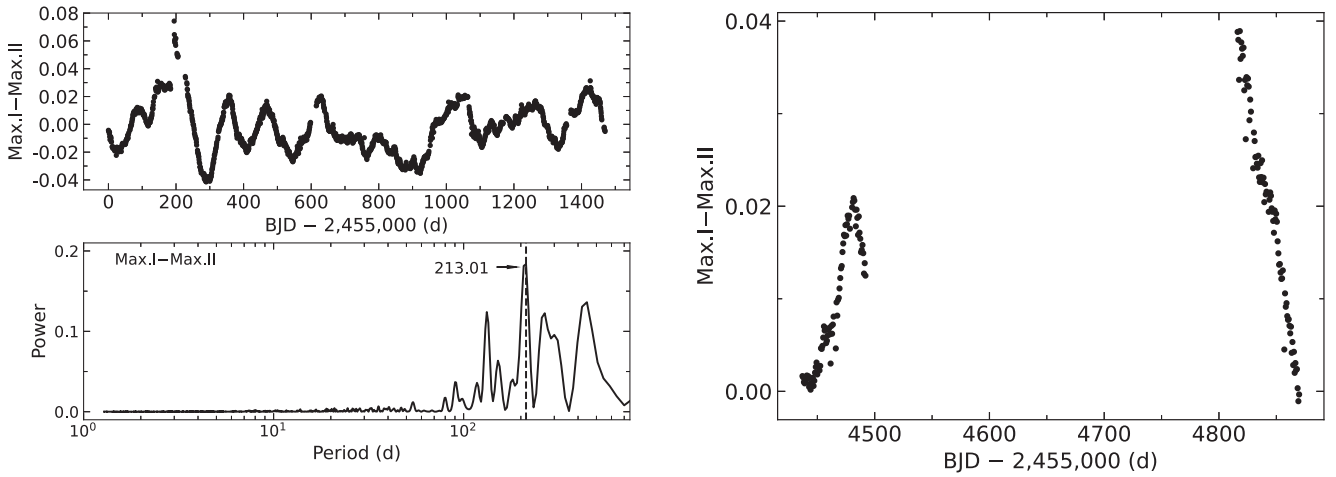
Figure 7. Right panel: the Max.I−Max.II evolving with time derived from Kepler data (upper panel) and the LS periodogram of the Max.I−Max.II (lower panel). Left panel: the Max.I−Max.II evolving with time derived from TESS data.
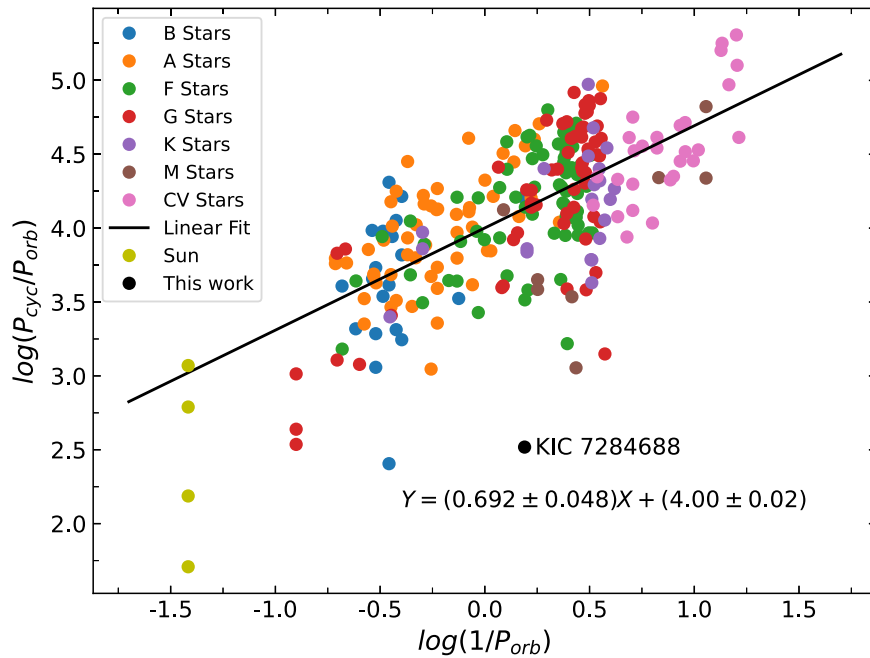
Figure 8. The $\log(P_{cyc}/P_{orb})$ vs. $\log(1/P_{orb})$ and a linear fit (black line) for EBs from Table 13 of Pi et al. (2019). EBs with different spectral types are represented by different colors and the CV represents cataclysmic variables.

found.) In the right panel of Figure 7, the Max.I−Max.II is almost always greater than zero, but there is a decreasing trend between days 4480 and 4500.

5. Discussion

The significant inequality in light maxima and the flares shown in Figure 1 and Figure 2 are probably caused by magnetic activity, supported by the evidence that both components of the EBs are solar-type stars. Furthermore, the rapid quasiperiodic modulations of ∼213 days ($P_{\mathrm{Max.I-Max.II}}$) detected in Max.I−Max.II are almost equal to the period of ∼207 days found in the $O−C$ diagram. The periodic behavior of the Max.I−Max.II may be connected either with magnetic cycle of the binary system or the longitude movements of starspots.

The scenario of the magnetic cycle of the binary system cannot be held responsible for the quasiperiodicity in the Max.I−Max.II, since the $P_{\mathrm{Max.I-Max.II}}$ is very short in comparison with EBs with magnetic cycles with timescales of a few years or decades. Pi et al. (2019) found a weak linear correlation between $\log(P_{cyc}/P_{orb})$ versus $\log(1/P_{orb})$ among EBs with rotation period less than 8 days, as shown in Figure 8, where the P_{cyc} is magnetic cyclic length, the P_{orb} is orbital periods of EBs in Table 13 of Pi et al. (2019), and the different color points represents EBs with different spectral types. We refit the data listed in Table 13 of Pi et al. (2019) with a linear function. Indeed, excepting the Sun with four solar activity cycles with different length, most of points on Figure 8 accord with the linear trend (black lines), which maybe hint that there exists a linear correlation between the two quantities as long as these binaries are short-period EBs. Under the assumption that the $P_{\mathrm{Max.I-Max.II}}$ comes from magnetic cycle of the binary system, we plot the point ($\log(1/P_{orb}) \sim 0.189$ day^{-1}, $\log(P_{\mathrm{Max.I-Max.II}}/P_{orb}) \sim 2.518$, black point) on Figure 8. Obviously, the black point deviates from the linear fit. Therefore, this scenario can be ruled out unless that the binary

system have multiple magnetic cycles just like the Sun with more than one cycle and the $P_{\mathrm{Max.I-Max.II}}$ is a short starspot activity cycle, similar to Rieger-type cycles (∼150 days) on the Sun (McIntosh et al. 2015). Therefore, this scenario can be ruled out.

Another scenario of the significant periodic behavior of the Max.I−Max.II is related to the longitude movements of starspots due to difference rotation. Using a spot model involving stellar differential rotation, Tran et al. (2013) interpreted the anticorrelations in the $O−C$ diagrams for the primary and secondary eclipse minima of close binaries as the longitude movements of starspots with timescales of a few months. Under the assumptions that the explanation is correct and that the period of 0.6440 days detected in out-of-eclipse residuals is the rotation period of starspot, the quasiperiod of ∼207 days seen in the $O−C$ periodogram is most likely a beat period between binary orbital period and the rotation period of starspot. More specifically, starspots with $P_{rot} = 0.6440$ days will effectively precede 360° (0°.6460 d - 0°.6440 d)/ 0°.6460 d=1°.1146 in each circle. The time for coming back to the same position is (360°/1°.1146)$P_{orb} \approx 323P_{orb} \approx 208.6$ days, namely beat period, which is close to the period in the $O−C$ periodogram. The results are consistent with the ones obtained by Balaji et al. (2015) using a method of phase tracking (see Figure 9 of Balaji et al. 2015); namely: the starspot is prograde with respect to the binary orbit (in a frame of reference rotating with the binary) and the time for starspot circling the star over one time is about 200 days. Since the period of ∼213 days in Max.I−Max.II is very close to the beat period, the rapid variable O'Connell effect may be due to the longitude movements due to difference rotation. Besides, the beat periods for the other two periods 0.6428 days and 0.6429 days in the Kepler residuals are approximately 130 days and 134 days, which corresponds to the spike of ∼130 days detected in the periodogram of Max.I−Max.II. Therefore, the oscillation in the Max.I−Max.II between days 300 and 700 is probably from the longitude movements due to difference

rotation. These evidences offer support for the longitude movements of starspots due to differential rotation. Therefore, this scenario could be responsible for the significant periodic behavior in the Max.I−Max.II.

In addition, another rapid oscillation (∼50 days) between days 1100 and 1200 in the Max.I−Max.II panel of Figure 7 is similar to the ones (∼50 days) detected in W UMa-type binary system, HH UMa and V410 Aur, which were explained by Wang et al. (2015) and Luo et al. (2017) using flip-flop cycle, a periodic switch of dominant activity level between two active longitudes on the opposite hemispheres. However, the inference of two active longitudes derived from light curves can be highly misleading (Basri & Shah 2020). Therefore, other observational studies, such as the Doppler imaging, are needed to confirm the inference.

Moreover, there are two additional signal with period longer than ∼213 days in the Max.I−Max.II periodogram (see Figure 7). Considering that starspots on late-type stars can be long-lasting with life timescales of years, the blurring signals may be related to the evolution of active region, eg. growth, decay.

6. Summary

The Kepler, TESS photometric and LAMOST spectroscopic analysis shows that KIC 7284688 is a triple-lined system composed of a nearly equal-mass solar-type eclipsing binary with a line-of-sight coincident star. The inequality of light curve at quadrature positions are most likely due to starspot activity. From the LS periodograms of the out-of-eclipse residuals, the $O-C$ diagram, the Max.I−Max.II, we identify that the period (∼213 days) of Max.I−Max.II is close to the beat between the orbital period (∼0.646 days) and the rotation period (∼0.644 days) of starspot, which is consistent with the periodic length derived from the $O-C$ diagram. Therefore, the variable O'Connell effect in the binary is likely connected to starspot migration and it is a rapid quasiperiodic variations in comparison with magnetic cycles with timescales of a few years or decades.

ORCID iDs

Yang Pan ⓘ https://orcid.org/0000-0001-8637-5492
Xiaobin Zhang ⓘ https://orcid.org/0000-0002-5164-3773

References

Astropy Collaboration, Robitaille, T. P., Tollerud, E. J., et al. 2013, A&A, 558, A33
Balaji, B., Croll, B., Levine, A. M., & Rappaport, S. 2015, MNRAS, 448, 429
Basri, G., & Shah, R. 2020, ApJ, 901, 14
Borucki, W. J., Koch, D., Basri, G., et al. 2010, Sci, 327, 977
Claret, A. 2017, A&A, 600, A30
Conroy, K. E., Prša, A., Stassun, K. G., et al. 2014, AJ, 147, 45
Czesla, S., Schröter, S., Schneider, C. P., et al. 2019, PyA: Python astronomy-related packages, Astrophysics Source Code Library, ascl:1906.010
De Cat, P., Fu, J. N., Ren, A. B., et al. 2015, ApJS, 220, 19
Fetherolf, T., Welsh, W. F., Orosz, J. A., et al. 2019, AJ, 158, 198
Frasca, A., Molenda-Żakowicz, J., Alonso-Santiago, J., et al. 2022, A&A, 664, A78
Fu, J., Zong, W., & Wang, H. 2022, SSPMA, 52, 289502
Fu, J.-N., Cat, P. D., Zong, W., et al. 2020, RAA, 20, 167
Gao, Q., Xin, Y., Liu, J.-F., Zhang, X.-B., & Gao, S. 2016, ApJS, 224, 37
Harris, C. R., Millman, K. J., van der Walt, S. J., et al. 2020, Natur, 585, 357
Hunter, J. D. 2007, CSE, 9, 90
Kirk, B., Conroy, K., Prša, A., et al. 2016, AJ, 151, 68
Knote, M. F., Caballero-Nieves, S. M., Gokhale, V., Johnston, K. B., & Perlman, E. S. 2022, ApJS, 262, 10
Kurucz, R. L., Furenlid, I., Brault, J., & Testerman, L. 1984, Solar Flux Atlas from 296 to 1300 nm (Sunspot, NM: National Solar Observatory)
Kwee, K. K., & van Woerden, H. 1956, BAN, 12, 327
Li, C.-q., Shi, J.-r., Yan, H.-l., et al. 2021, ApJS, 256, 31
Lucy, L. B. 1967, ZAp, 65, 89
Luo, X., Wang, K., Zhang, X., et al. 2017, AJ, 154, 99
Lurie, J. C., Vyhmeister, K., Hawley, S. L., et al. 2017, AJ, 154, 250
McIntosh, S. W., Leamon, R. J., Krista, L. D., et al. 2015, NatCo, 6, 6491
McKinney, W. 2010, in Proc. the 9th Python in Science Conf., ed. S. van der Walt & J. Millman (Austin, TX: SciPy), 56
O'Connell, D. J. K. 1951, PRCO, 2, 85
Pan, Y., Fu, J.-N., Zhang, X.-B., Wang, J.-X., & Li, C.-Q. 2022, RAA, 22, 075014
Pi, Q.-f., Zhang, L.-y., Bi, S.-l., et al. 2019, ApJ, 877, 75
Prša, A., Batalha, N., Slawson, R. W., et al. 2011, AJ, 141, 83
Prša, A., & Zwitter, T. 2005, ApJ, 628, 426
Reback, J., McKinney, W., Jbrockmendel, et al. 2020, pandas-dev/pandas: Pandas v1.0.3, Zenodo, doi:10.5281/zenodo.3509134
Ricker, G. R., Winn, J. N., Vanderspek, R., et al. 2015, JATIS, 1, 014003
Roettenbacher, R. M., Kane, S. R., Monnier, J. D., & Harmon, R. O. 2016, ApJ, 832, 207
Ruciński, S. M. 1969, AcA, 19, 245
Rucinski, S. M. 2002, AJ, 124, 1746
Rucinski, S. M. 2004, in IAU Symp. 215, Stellar Rotation, ed. A. Maeder & P. Eenens (San Francisco, CA: ASP), 17
Shi, X.-d., Qian, S.-b., Li, L.-j., & Liu, N.-p 2021, AJ, 161, 46
Slawson, R. W., Prša, A., Welsh, W. F., et al. 2011, AJ, 142, 160
Sriram, K., Malu, S., Choi, C. S., & Vivekananda Rao, P. 2017, AJ, 153, 231
Tran, K., Levine, A., Rappaport, S., et al. 2013, ApJ, 774, 81
van Hamme, W. 1993, AJ, 106, 2096
Wang, K., Zhang, X., Deng, L., et al. 2015, ApJ, 805, 22
Wilsey, N. J., & Beaky, M. M. 2009, SASS, 28, 107
Wilson, R. E. 1979, ApJ, 234, 1054
Wilson, R. E. 1990, ApJ, 356, 613
Wilson, R. E. 2012, AJ, 144, 73
Wilson, R. E. 2020, ApJS, 251, 15
Wilson, R. E., & Devinney, E. J. 1971, ApJ, 166, 605
Zhang, B., Li, J., Yang, F., et al. 2021, ApJS, 256, 14
Zong, W., Fu, J.-N., De Cat, P., et al. 2018, ApJS, 238, 30